Water Research X 30 (2026) 100496

Contents lists available at ScienceDirect

Water Research X

journal homepage: www.sciencedirect.com/journal/water-research-x

Chain-length-dependent adsorption of extracellular DNA on biochar: Behaviors, mechanisms, and structural Stability

Xiao Sun [a], Lin Shi [b,*], Huang Zhang [b], Fangfang Li [a], Yanjin Long [c], Di Zhang [a,b,*]

[a] Yunnan Provincial Key Laboratory of Soil Carbon Sequestration and Pollution Control, Faculty of Environmental Science and Engineering, Kunming University of Science and Technology, Kunming, 650500, China
[b] College of Resources and Environment, Linyi University, Linyi, 276005, China
[c] Yunnan Zhipin Agricultural Science and Technology Co., Ltd, Kunming, 650500, China

ARTICLE INFO

Keywords:
Adsorption
Desorption
DNA
Conformational change

ABSTRACT

The environmental fate of extracellular DNA is significantly influenced by its interaction with widely used biochar. However, a systematic understanding of how DNA chain length and biochar properties jointly govern the adsorption process, mechanism, and subsequent DNA stability remains limited. This study systematically investigated the adsorption behaviors and mechanisms of short-stranded (sDNA) and long-stranded DNA (LDNA) on biochars produced at 300 – 600°C under neutral pH conditions. sDNA exhibited a higher adsorption capacity (5.91 mg g^{-1} on BC600) by accessing internal mesopores on biochar, whereas LDNA showed a lower adsorption (2.22 mg g^{-1} on BC600) and a stronger desorption hysteresis, resulting from multisite anchoring with biochars. The release rate values of sDNA and LDNA were 5 – 20% and 4 – 13% respectively on BC300. Correlation studies and desorption experiments revealed that π-π interactions and hydrophobic forces were the primary adsorption mechanisms. Spectroscopic analyses and molecular dynamic simulation confirmed conformational changes in the adsorbed DNA but showed no chain fragmentation. These findings underscore that DNA chain length and biochar properties jointly govern the sequestration and stability of DNA, providing essential mechanistic insights for assessing the role of biochar in the persistence and mobility of genetic material in the environment.

1. Introduction

Biochar, a carbon-rich material produced from the pyrolysis of biomass under oxygen-limited conditions, has garnered significant attention for its multifunctional roles in carbon sequestration, soil amendment, and environmental remediation (Song et al., 2024; Yang et al., 2022b). Its widespread application leads to its inevitable interaction with various environmental contaminants and biomolecules, including extracellular DNA (eDNA) (Hao et al., 2024; He et al., 2023; Lian et al., 2020). eDNA is a ubiquitous and persistent component in soil and aquatic environments, playing a critical role in horizontal gene transfer, which facilitates the spread of resistance genes and influences microbial community evolution (Wu et al., 2025; Zhang et al., 2024). Understanding the interactions between eDNA and biochar is therefore fundamentally important for assessing the environmental fate of DNA, particularly its mobility, persistence, and potential bioavailability.

The adsorption of DNA on carbonaceous materials, such as graphene oxide and activated carbon, has been previously investigated, with studies suggesting that interactions including π-π stacking, hydrogen bonding, and electrostatic forces are involved (Shao et al., 2022; Yu et al., 2017). However, as a highly heterogeneous material, the adsorption capacity and mechanism of biochar are strongly influenced by its physicochemical properties, which are in turn dictated by the pyrolysis temperature and biomass source (Xiao et al., 2018). For instance, high-temperature biochars typically possess a higher specific surface area (SSA), greater aromaticity, and fewer oxygen-containing functional groups, which may lead to a stronger affinity for biomolecules like DNA compared to low-temperature biochars (Yang et al., 2022a). Fang et al. found that the biochar prepared from wood chip exhibited a higher adsorption for DNA than that prepared from wheat straw and peanut shell. This result was attributed to the larger external surface area and pore size of wood chip-based biochar (Fang et al., 2021). While several studies have investigated the adsorption capacity and mechanism of DNA on biochar (Lian et al., 2020; Wu et al., 2022), a systematic evaluation of how biochar properties dictate the adsorption kinetics, capacity, and underlying mechanisms for DNA of different

* Corresponding authors.
E-mail addresses: shilin@lyu.edu.cn (L. Shi), zhangdi2002113@lyu.edu.cn (D. Zhang).

https://doi.org/10.1016/j.wroa.2026.100496
Received 6 December 2025; Received in revised form 11 January 2026; Accepted 16 January 2026
Available online 17 January 2026

molecular sizes remains insufficient.

A critical but often overlooked factor is the length of eDNA strand. In natural environment, eDNA exists in a spectrum of sizes, from short oligonucleotides to long genomic fragments (Ballard and Whitlock, 2004; Blackman et al., 2024). Over extended time, highly fragmented short DNA (< 100 bp) dominates in environment (Overballe-Petersen et al., 2013; Sawyer et al., 2012). Chain length directly influences diffusion coefficients and accessibility to adsorption sites. Previous researches on mineral have indicated that longer DNA strands may exhibit stronger adhesion due to multi-site attachment, while shorter strands might access more confined pores (Cochran et al., 2024; Wang et al., 2022; Zhang et al., 2021). Furthermore, adsorption at mineral surfaces modifies the DNA conformation, probably impeding molecular recognition by enzymes, which effectively hinders enzymatic degradation (Cai et al., 2006; Nguyen and Elimelech, 2007). The adsorption of DNA on minerals and biochars exhibited fundamental differences in its main mechanisms. The adsorption of DNA on mineral was primarily driven by electrostatic interactions and cation bridging. The adsorption mechanism of DNA on biochar was diverse and include non-electrostatic forces such as π-π interactions between the aromatic structure of biochar and DNA bases, as well as hydrophobic interactions (Shi et al., 2024). Nevertheless, a knowledge gap exists in comprehending the chain-length-dependent adsorption behavior on biochar, including the associated changes in DNA conformation and stability upon binding. Such understanding is crucial for predicting the potential of biochar to act as a sink or a vector for genetic material in the environment.

The primary objectives of this study were therefore to (1) determine the adsorption characteristics (including kinetics and isotherms) of sDNA and LDNA on biochars produced at different temperatures; (2) elucidate the dominant adsorption mechanisms and their dependence on both DNA length and biochar properties through correlation analysis and desorption experiments; and (3) clarify the structural integrity and stability of the adsorbed DNA using spectroscopic techniques and molecular dynamics simulations. We hypothesize that sDNA and LDNA exhibit distinct adsorption behaviors due to differences in steric hindrance and multi-site anchoring, leading to divergent environmental fates. The findings of this work will provide novel insights into the molecular-level interactions between DNA and engineered biochars, which is essential for assessing the ecological impacts of biochar application and its role in controlling the spread of antibiotic resistance.

2. Materials and methods

2.1. Materials

Herring sperm DNA (sDNA, ~ 40 bp, ~ 13.6 nm) and salmon sperm DNA (LDNA, > 2000 bp, > 680 nm) were used as models for short-chain and long-chain DNA, respectively. Both types of DNA exhibited the characteristic double-helix structure and have been widely employed in studies investigating interactions with adsorbents (Kjaer et al., 2022; Yang et al., 2022a). The structures of tested DNA were characterized by Fourier transform infrared spectroscopy (FTIR, Variance 640-IR, USA), as shown in Fig. S1(a). Characteristic peaks of B-form DNA were observed at 1227, 965, 834, and 783 cm^{-1} (Banyay et al., 2003). The peak positions and corresponding conformational band assignments of infrared spectra of DNA were provided in Table S1. To maintain a stable pH conditions throughout the experiments and prevent structural alterations of DNA induced by pH fluctuations, all DNA solutions were prepared in 10 mmol L^{-1} Tris-HCl buffer at pH = 7. The purity of tested DNA was determined using a UV–Vis spectrophotometer (Shimadzu UV-2600). As shown in Fig. S1(b), both sDNA and LDNA exhibited a characteristic absorption peak at 260 nm, with absorbance ratio at 260 and 280 nm (A_{260}/A_{280}) ranging between 1.8 and 1.9, confirming that the purity of tested DNA met the experimental requirements. The diameter of B-form DNA is approximately 2 nm.

NaOH, NaH_2PO_4, Na_2HPO_4, urea, and methanol were of analytical grade and purchased from Aladdin. Tris (2-amino-2-(hydroxymethyl)-propane-1,3-diol) and DMPO (5,5-dimethyl-1-pyrroline-N-oxide) were procured from BioFroxx and Sigma-Aldrich, respectively. Ultrapure water was used throughout the experiments.

2.2. Preparation and characterization of biochar

The collected corn stalk was rinsed to remove impurities, cut into pieces, and dried in an oven at 60°C. The corn stalk pieces were carbonized in a N_2-purged muffle furnace for 4 hours, when the pyrolysis temperature reached to 300, 400, 500, and 600°C, followed by slow cooling. Each biochar was prepared in a single batch. The obtained biochar was ground and sieved through a 100-mesh screen (< 150 μm), and then the raw biochars were repeatedly rinsed via vacuum filtration (0.45 μm membrane) with ultrapure water. The size range of obtained biochar powder was 0.45 - 150 μm. Finally, the resulting biochar powder was freeze-dried and labeled as BC300, BC400, BC500, and BC600, respectively.

The SSA and pore size distribution were determined with a surface area analyzer (BET, Micromeritics ASAP 2020, USA). Prior to the test, samples were degassed under vacuum at 120 °C for 12 h to remove surface volatile impurities. N_2 adsorption-desorption test were performed in a liquid N_2 environment at 77.30 K, and adsorption data were collected using a relative pressure range of 0.01 to 0.99. The BET surface area was calculated using the multi-point BET equation in the relative pressure range $P/P_0 = 0.01$ to 0.30, and the value of *C* (BET constant) was positive to satisfy the Rouquerol consistency criteria. Raman spectroscopy (BX41, HOEIBA Scientific, France) was employed to characterize the defect structures and graphitization degree of the biochar. The elemental composition was quantified using an elemental analyzer (Elementar MicroCube, Germany) and X-ray photoelectron spectroscopy (XPS, Thermo Scientific K-Alpha, USA). Ash contents were determined by calculating the mass difference before and after calcination at 750°C with continuous air supply for 4 hours in a muffle furnace. Functional groups on biochar surface were identified by FTIR. The zeta potential was measured using a zeta potential analyzer (ZetaPlus, Brookhaven, USA).

2.3. Batch adsorption experiments

Adsorption kinetics and isotherm experiments were conducted at 25°C using a 10 mmol L^{-1} Tris-HCl buffer (pH = 7) as background solution. For the kinetic studies, 20 mL of 80 mg L^{-1} sDNA or LDNA solution was added to 40 mL amber vials containing 20 mL of 100 mg biochar suspension. The biochar suspension had been pre-adjusted to pH = 7, with pH fluctuations maintained within ± 0.3 during the experiments. The mixtures were shaken at 170 rpm and 25°C. Sampling was performed at predetermined time intervals (0.5, 1, 2, 4, 8, 12, 24, 30, 36, and 48 h): 3 mL aliquots were collected and filtered through 0.45 μm polyethersulfone membranes. The initial 1 mL filtrate was discarded, and the subsequent filtrate was analyzed using a UV spectrophotometer to determine DNA concentration based on absorbance at 260 nm. Preliminary experiments confirmed that the 0.45 μm membranes effectively retained suspended biochar particles, and discarding the initial 1 mL filtrate eliminated any potential interference with DNA concentration measurements. Blank controls (biochar suspension without DNA) were subjected to the same procedures, and UV absorbance at 260 nm was measured. The absorbance of experimental group was subtracted from that of the blank control group to minimize the quantitative error blank. sDNA/LDNA standard solutions (10-40 mg L^{-1}) were spiked into biochar suspension, and spike-recovery rates were calculated. The spike-recovery rates of sDNA and LDNA were 97.53-118.67% and 99.53-126.36%, respectively, indicating the reliability and applicability of UV260 for detecting DNA in dissolved organics from biochars (data shown in Table S2).

For adsorption isotherms, 4 mL of sDNA or LDNA with a series of

concentrations (4-120 mg L^{-1}) was added to 8 mL amber vials containing 4 mL of 20 mg biochar suspension. After 48 h of equilibration, the supernatant of samples was collected after centrifugation (4000 rpm for 15 min), and filtered for DNA concentration measurements.

The pseudo-first- kinetics model, second-order kinetics model, and intraparticle diffusion model (IDM) were employed to fit the adsorption kinetics. The adsorption isotherms were fitted by the Langmuir and Freundlich models. The detailed equations are provided in the Supplementary materials (Text S1).

2.4. Batch desorption experiment

The desorption of sDNA and LDNA from biochar was evaluated using different eluents to investigate the dominant interaction mechanisms: 10 mmol L^{-1} Tris-HCl, 20 mmol L^{-1} NaOH, 0.10 mol L^{-1} phosphate buffer (pH = 7) prepared by mixing Na_2HPO_4 and NaH_2PO_4, 2 mol L^{-1} urea solution, and 20% (v/v) methanol solution. Initially, both sDNA and LDNA solutions were prepared at an initial concentration of 80 mg L^{-1}, and the adsorption equilibrium procedure followed the same protocol as the adsorption isotherm experiments. After reaching adsorption equilibrium, the samples were centrifuged at 4000 rpm for 15 min, and 6 mL of supernatant was collected to determine the equilibrium concentration. Then, 6 mL of the corresponding desorption solution was added to the remaining 2 mL sample. The mixtures were shaken under the same conditions as the adsorption experiments until desorption equilibrium was achieved (48 h for sDNA and 12 h for LDNA). Subsequently, 3 mL aliquots were filtered, and the DNA concentration was determined using calibration curves specifically established for each desorption solution. Preliminary data confirmed that the characteristic absorption peak of DNA remained detectable at 260 nm in all five desorption solutions.

For the desorption experiments following the adsorption isotherm tests, the samples were centrifuged at 4000 rpm for 15 min after adsorption equilibrium, and 7 mL of supernatant was removed for equilibrium concentration measurement. An equal volume of the adsorption background solution was then added to replace the removed supernatant. The mixtures were shaken under identical adsorption conditions, with desorption equilibrium times of 48 h for sDNA and 12 h for LDNA, before determining the DNA concentration as described. This desorption cycle was repeated twice to obtain two consecutive desorption isotherms.

2.5. Characterization after adsorption

Both sDNA and LDNA solutions were prepared at an initial concentration of 120 mg L^{-1} and subjected to the adsorption kinetic procedure described above. After reaching adsorption equilibrium, the samples were centrifuged at 4000 rpm for 15 min. Then, 36 mL of supernatant was collected and retained. Subsequently, the remaining BC-DNA suspension was washed twice with 36 mL of background solution. The resulting samples were freeze-dried and labeled as BC300-sDNA, BC400-sDNA, BC500-sDNA, BC600-sDNA, BC300-LDNA, BC400-LDNA, BC500-LDNA, and BC600-LDNA.

For FTIR spectroscopy, approximately 1 mg of biochar (before and after DNA adsorption) was mixed with 200 mg of dried KBr powder. The mixtures were homogenized using an agate mortar and pressed into pellets. FTIR spectra were recorded over the range of 400–4000 cm^{-1} with 32 accumulated scans. The synchronous two-dimensional correlation spectroscopy (2D-COS) was employed to solve the problems of peak overlapping. The data set was analyzed using 2D Shige software (Kwansei-Gakuin University, Japan).

For electron paramagnetic resonance (EPR) analysis, about 2 mg of biochar (before and after DNA adsorption) was loaded into quartz capillaries (707-SQ-250M, Wilmad, USA) to measure signals of persistent free radicals (PFRs). The EPR measurements were performed using the following parameters: microwave power 10 mW, frequency 9.86 GHz, scan time 102.4 s, center field 3520 G, and sweep width 400 G.

To detect ·OH radicals, a 100 mmol L^{-1} DMPO (5,5-dimethyl-1-pyrroline N-oxide) solution was prepared in PBS buffer. Then, 500 μL of DMPO solution was mixed with 5 mg of biochar (before and after DNA adsorption), vortexed for 1 min, and filtered through a 0.45 μm membrane. A 25 μL aliquot of the filtrate was transferred into an EPR capillary, with the tip sealed using grease, and inserted into an EPR quartz tube for measurement. For $O_2^{\cdot-}$ detection, the same procedure was followed using a 100 mmol L^{-1} DMPO solution prepared in methanol.

For agarose gel electrophoresis, 18 μL of the supernatant collected after adsorption equilibrium was mixed with 9 μL of 6 × loading buffer. The mixtures were loaded onto a 1% agarose gel and separated at 5 V cm^{-1}. Electrophoresis was terminated when bromophenol blue and xylene cyanol FF had migrated to appropriate distances. The gel was then visualized and photographed using a uVP gel imaging system. For sDNA analysis, high-resolution polyacrylamide gel electrophoresis was performed at 60 W for 30 min, followed by silver staining, gel washing, drying, and imaging.

Molecular dynamics (MD) simulations provided a powerful method to study the conformation dynamics and spatial structural changes. It was employed to analyze the stability of DNA during the adsorption process, and the simulation details were displayed in Text S2.

3. Results and discussion

3.1. Characterization of biochars

Fig. 1 (a) displayed the N_2 adsorption-desorption isotherms of biochars prepared at four different pyrolysis temperatures. All biochars exhibited type IV isotherms as classified by IUPAC, indicating the pore structure of tested biochars was mainly mesoporous (Qi et al., 2017). The pore size distribution of biochars was calculated using the Barrett–Joyner–Halenda method based on desorption breach date, and the results were showed in Fig. 1 (b). Although tested biochars had similar pore structures, the mesopore (2-5 nm) areas and volumes of BC600 were much higher than those of BC300, BC400 and BC500. The mesopore volume of BC600 was 0.0318 $cm^3\ g^{-1}$, which was 9.1-fold, 4.6-fold, and 1.8-fold higher than those of BC300, BC400, and BC500, respectively. In addition, the mesopore volume accounted for 53.85 – 74.47% of the total pore volume, signifying that biochars were a mesoporous material (Table 1). The microporous features of biochars were evaluated using the t-plot method. N_2 adsorption have limited diffusion into narrow micropores (< 0.7 nm) at 77 K, potentially leading to an underestimation of micropore volume. As the pyrolysis temperature increased, SSA of biochars increased, while average pore diameter (D_A) decreased, with related parameters summarized in Table 1. The sharp increase in SSA of BC600 (112.95 $m^2\ g^{-1}$) was attributed to the following factors: (1) This temperature reached the decomposition threshold for tar and hydrocarbon compounds, which were transformed gases (CH_4, CO, H_2) and escaped, resulting in formation of micropores. (2) Aromatization and polycondensation reactions within the carbon framework generated new slit-shaped micropores (Xiao et al., 2018).

Raman spectroscopy further characterized the defect structure and graphitization of biochars (Fig. 1 (c)). Two distinct bands were observed at around 1356 cm^{-1} (D band) and 1588 cm^{-1} (G band), which signified sp^3 carbon vibrations at edges or defects and in-plane sp2 carbon vibrations in graphitic structures, respectively (Teng et al., 2019). The intensity ratio of the D band to the G band (I_D/I_G) often served to describe the biochar structural disorder. The I_D/I_G ration of all biochars showed only minor differences, indicating that the defect degree in all biochars was almost identical.

The bulk and surface elemental composition of biochars were analyzed using elemental analysis and XPS (Fig. 1 (d) and S2), with the results summarized in Table 1. The molar ratio, ash contents and Zeta potential at pH ~ 7 of biochar were also displayed in Table 1. As the pyrolysis temperature increased, the C and ash content of biochars

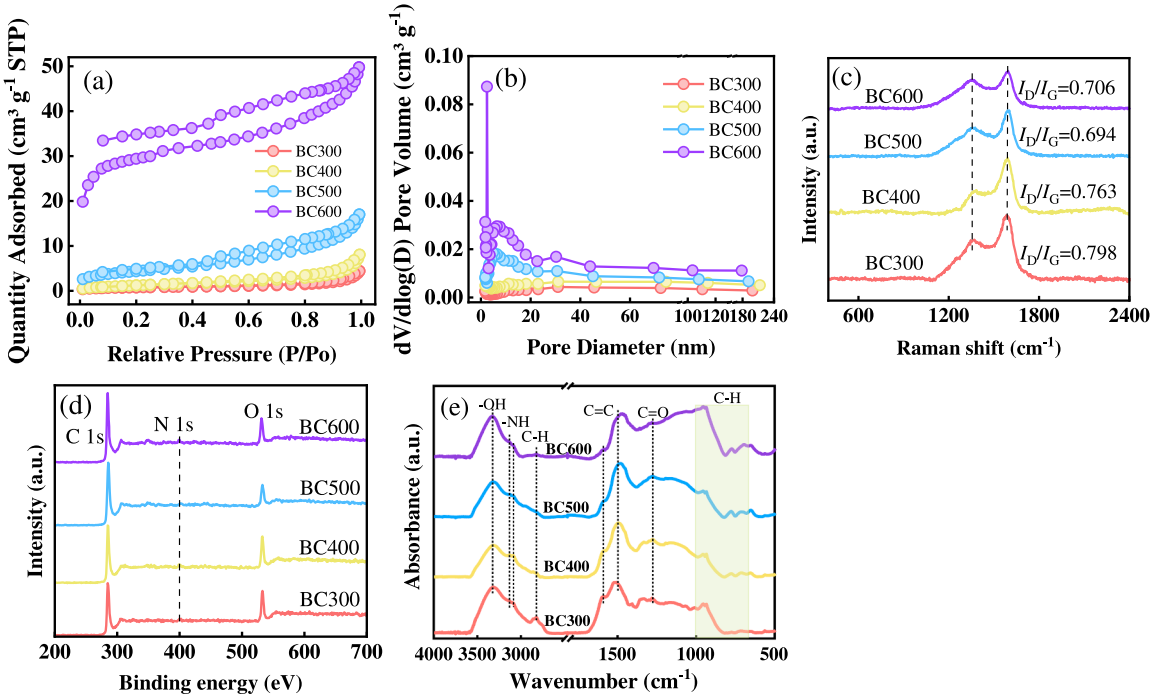

Fig. 1. The N_2 adsorption-desorption isotherms (a), pore-size distribution (b), Raman spectra (c), XPS survey spectra (d), and FTIR spectra (e) of tested biochars.

Table 1
The physicochemical characteristics of tested biochars.

Biochar	SSA_{BET}	SSA_{Micro}	SSA_{Micro}/SSA_{BET}	V_{total}	V_{Micro}	V_{meso}	V_{Micro}/V_{total}	V_{meso}/V_{total}	D_A	Ash
	$m^2\ g^{-1}$	$m^2\ g^{-1}$	%	$cm^3\ g^{-1}$	$cm^3\ g^{-1}$	$cm^3\ g^{-1}$	%	%	nm	%
BC300	2.85	0.99	35.74	0.0065	0.0004	0.0035	0.62	53.85	9.57	3.70
BC400	5.01	0.52	10.38	0.0124	0.0001	0.0069	0.81	55.65	9.95	17.20
BC500	15.71	2.55	16.23	0.0245	0.0010	0.0177	4.08	72.24	5.64	4.28
BC600	112.95	85.21	75.44	0.0427	0.0048	0.0318	11.24	74.47	2.73	21.77

	Bulk elemental content (%)				Surface elemental content (%)			Molar ratio		Zeta potential		pH
	C	H	O	N	C^S	O^S	N^S	H/C	(O+N)/C	$(O+N)/C^S$	mV	
BC300	58.95	3.23	13.67	2.15	56.63	37.85	5.52	0.66	0.21	0.58	-41.51	6.80
BC400	60.93	2.68	10.76	2.19	70.86	24.64	4.50	0.53	0.16	0.32	-41.36	6.89
BC500	63.40	1.94	8.18	2.05	75.10	20.83	4.07	0.37	0.12	0.25	-35.48	6.98
BC600	64.57	1.14	6.03	1.78	79.80	17.52	2.68	0.21	0.09	0.19	-31.54	7.08

increased, whereas the contents of H, O, and N decreased. The higher C and O content on biochars surface compared with the bulk composition implied that the minerals of biochars were likely covered by organic matter as well as the heterogeneous spatial arrangement of composition within biochars (Sun et al., 2013). The H/C and (O+N)/C molar ratio of biochars reflected the degree of aromatic condensation and polarity, respectively (Chen et al., 2019). The lower H/C value of BC600 suggested the formation of a highly carbonized biochar at this pyrolysis temperature. The decreasing trends of H/C and (O+N)/C indicated that high-temperature pyrolysis promoted the generation of biochar with enhanced aromaticity and reduced polarity (Fan et al., 2019). The loss of polar functional groups also led to a decrease in surface negative potential during pyrolysis (Table 1). As could be seen from XPS spectra (Fig. S2), most of carbon atoms on biochar surface existed in the form C-C. The proportion of C-C on biochar surface increased and the proportion of C-O and C=O decreased with the increase of pyrolysis temperature, indicating that the total amount of oxygen-containing functional groups on biochar surface decreased and the aromaticity of biochar increased with the increase of pyrolysis temperature, which was consistent with the results of elemental analysis. The N 1s spectra of biochar included two peaks that were attributed to pyridine N and pyrrole N (Chen et al., 2021).

The FTIR spectra were employed to analyze the functional groups of biochars (Fig. 1 (e)). The peak at 3385 cm^{-1} was attributed to –OH stretching in biochars. As the pyrolysis temperature increased, the absorption intensities at 2920, 2850, 1367and 1068 cm^{-1} decreased. These reductions imparted decreased polarity and a concomitant increase in aromaticity (Hu et al., 2021). The biochars exhibited skeletal vibrations of aromatic C=C bonds at 1594 cm^{-1}, suggesting the presence of relatively stable aromatic compounds or graphitic structures, which facilitated the adsorption of organic pollutants via π–π interactions.

3.2. Adsorption kinetics of sDNA and LDNA on biochars

We investigated adsorption kinetics of sDNA and LDNA on biochars at an initial concentration of 40 mg L^{-1} at pH 7 (Fig. 2). The adsorption of sDNA on tested biochars was fast in the first 2 h and reached equilibrium within 24 h (Fig. 2 (a)), and sorption of LDNA on tested biochars was fast in the first 1 h and reached equilibrium within 8 h (Fig. 2 (c)). All kinetic curves were fitted by PFO and PSO models, and relevant parameters were list in Table S3. Compared with the PFO model, the PSO model exhibited superior fitting performance for all curves as indicated by the

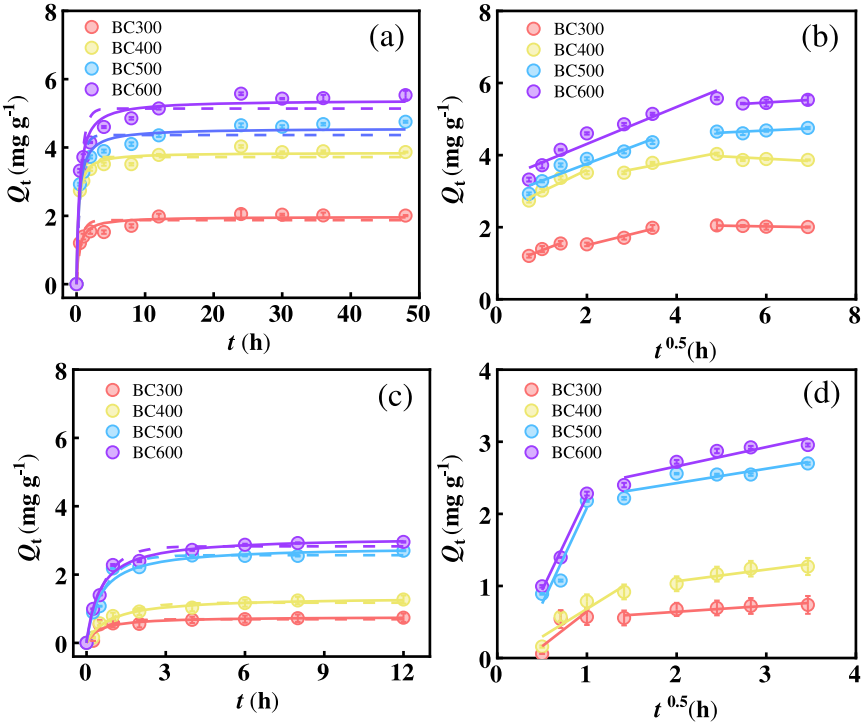

Fig. 2. Adsorption kinetics of sDNA (a, b) and LDNA (c, d) on biochars with IDM model fitting (b, d): Pseudo-first-order model (solid curves), Pseudo-second-order model (long-dashed curves). Data points and error bars represented the mean and standard deviation of triplicates run in parallel.

higher R^2_{adj} values ($\geq$ 0.89) and the negligible discrepancy between the experimental sorption quantity and the predicted Q_e at equilibrium. The adsorption rate of sDNA was slower than that of LDNA, but the adsorption capacity of sDNA on biochars was higher than that of LDNA. The similar phenomenon had been reported in previous studies (Lee et al., 2016; Zhang et al., 2021), which could be attributed to their different integration and diffusion processes. The shorter chain and smaller dimension of sDNA enabled it to ultimately integrate within the mesoporous biochar, resulting in higher capacity. However, the process of diffusing into these narrow pores was kinetically slower. On the other hand, the sorption of LDNA was primarily governed by its larger molecular size and steric hindrance, which prevents pore entry but allows for quicker attachment to open external sites, leading to a faster initial rate but limited overall capacity.

The IDM was employed to provide insights into the mechanisms and rate-limiting phases during the adsorption process of the DNA on biochars (Fig. 2 (b) and (d)), with fitting results shown in Table S3. The adsorption kinetics of sDNA on BC300 and BC400 were divided into three stages: (1) diffusion in boundary layer; (2) intraparticle diffusion; (3) adsorption equilibrium; while the adsorption kinetics of sDNA on BC500 and BC600 only contains the diffusion in boundary layer and adsorption equilibrium stages (Viet Cuong et al., 2022). The results might be attributed be the mesoporous and macroporous structure of the low-temperature biochar, which were more compatible with the size of sDNA. The adsorption kinetics of LDNA on the four biochars exhibited two stages, suggesting that the adsorption of LDNA was limited to the outer surface of biochars. The limited accessibility of LDNA to the internal sorption sites within biochar pores accounts for its inferior adsorption capacity relative to sDNA. The higher value of fitting slope (k_{p1}) for LDNA on biochar than that for sDNA indicats that LDNA diffused through the boundary layer faster than sDNA. LDNA had more nitrogenous bases, which led to a stronger affinity between LDNA and biochar due to the π-π interactions, which accelerates the adsorption.

3.3. Adsorption isotherm of sDNA and LDNA on biochars

Adsorption isotherms of different length DNA on biochars were determined at pH 7 (Fig. 3). Freundlich and Langmuir model were used to fit the isotherms of sDNA (Fig. 3 (a)) and LDNA (Fig. 3 (b)) adsorption on biochars, and the fitting parameters were presented in Table S4. The Freundlich model (R^2_{adj} > 0.90) was more suitable than the Langmuir model for describing the adsorption of DNA on biochars, suggesting that the adsorption was multilayer on a heterogeneous surface (Li et al., 2025). With pyrolysis temperature increasing, the adsorption capacities of sDNA and LDNA on biochars were increased, which was consistent with previous studies (Yang et al., 2022a). These results could be attributed to three primary factors: (1) The high-temperature biochar (BC500 and BC600) had higher SSA and mesopore volume than low-temperature biochar (BC300 and BC400), thereby providing more potential adsorption sites for DNA; (2) The high-temperature biochar had high aromaticity, which strengthened π-π interactions with DNA bases; (3) The high-temperature biochar carried less surface negative charge, which diminished the electrostatic repulsion with the negatively charged phosphate backbone of DNA and thus further promoting adsorption.

A comparison of the adsorption of sDNA and LDNA on same biochar revealed a higher adsorption capacity for sDNA. The smaller sDNA could more readily access pores of matching sizes, allowing interaction with a greater number of adsorption sites. Conversely, a larger LDNA occupied more surface binding sites (Fig. S3). Furthermore, steric hindrance between adsorbed LDNA molecules further hindered adsorption (Lv et al., 2024).

3.4. Adsorption mechanism of sDNA and LDNA on biochars

To tentatively identify possible factors influencing DNA adsorption, we conducted correlation analysis between DNA adsorption quantities (Q_e measured at C_0 = 40 mg·L^{-1}) and physicochemical properties of biochars (Fig. 4). The Q_e of sDNA was significantly negatively correlated with the H/C and (O+N)/C of biochars (Fig. 4 (a)), which might suggest

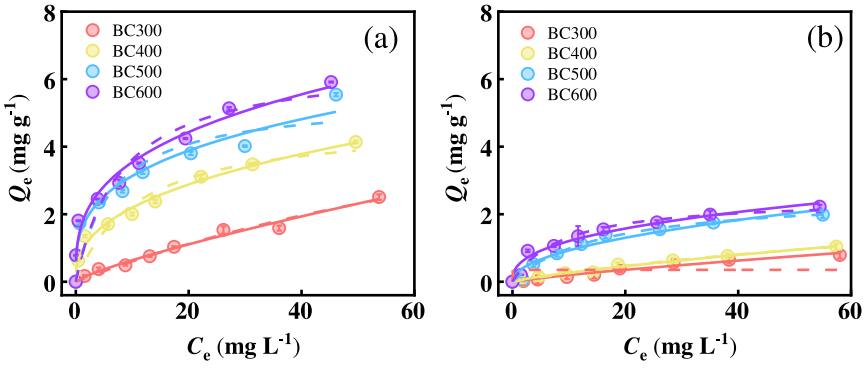

Fig. 3. Adsorption isotherms of sDNA (a) and LDNA (c) on biochars: Freundlich model (solid curves) and Langmuir model (long-dashed curves). Data points and error bars represented the mean and standard deviation of triplicates run in parallel.

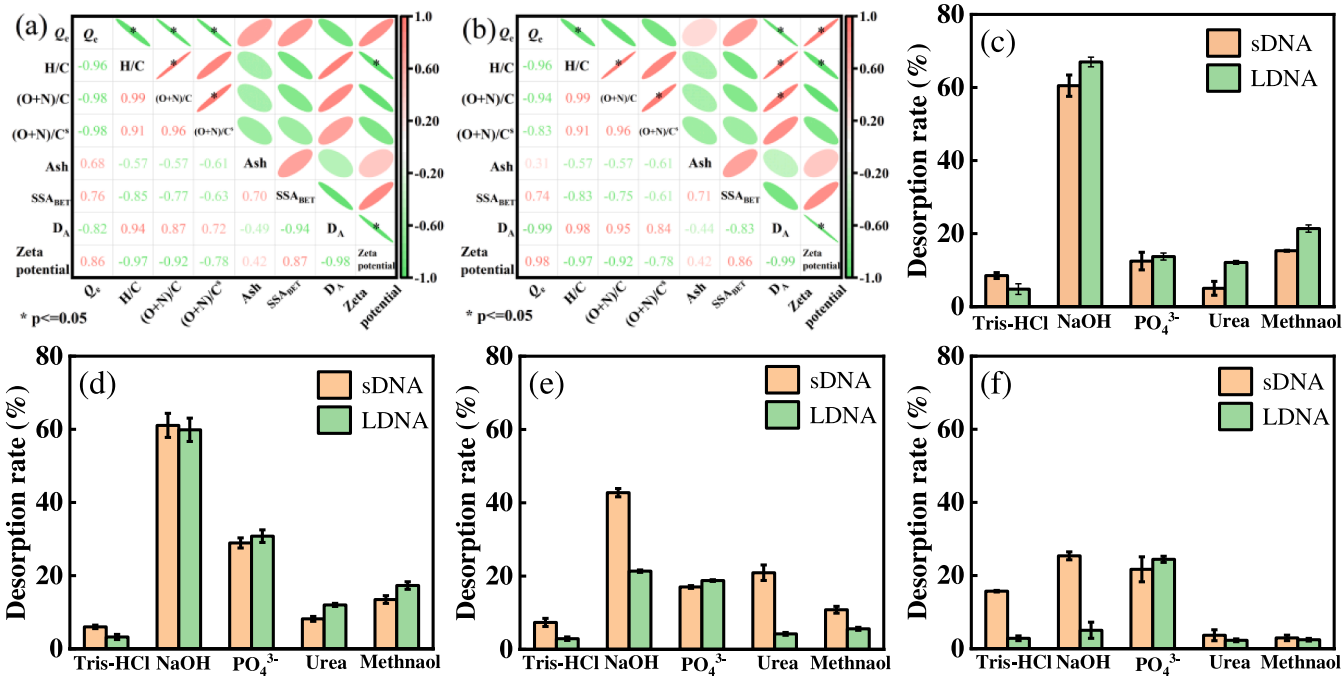

Fig. 4. Pearson correlation analysis between physicochemical properties of biochars (n = 4) and adsorption quantities (Q_e measured at C_0 = 40 mg L^{-1}) of sDNA (a) and LDNA (b). The colors red and green represent positive and negative correlations, respectively. All correlation analyses were performed with a confidence level of 95%. Desorption rate of sDNA and LDNA from BC300 (c), BC400 (d), BC500 (e) and BC600 (f) by different desorption solution. Data points and error bars represented the mean and standard deviation of triplicates run in parallel.

that π-π interaction and hydrophobic interaction could contribute to sDNA adsorption. A moderate correlation between SSA and Q_e indicated that a larger SSA might provide more adsorption sites, potentially benefiting DNA adsorption. Furthermore, a positive correlation trend between Zeta potential/ash content and Q_e might correspond to reduced electrostatic repulsion (as Zeta potential increases) and potential cation bridging/coordination effects from ash-borne metal ions, though these links remain speculative.

The Q_e of LDNA was significantly negatively correlated with H/C of biochars (Fig. 4 (b)), indicating that the π-π interaction could be a relevant mechanism for DNA adsorption on biochars, and it was not affected by the length of DNA. LDNA exhibited a weaker correlation between Q_e and (O+N)/C (R = -0.94) compared to sDNA (R = -0.98); one possible explanation was that LDNA's longer chain enhanced hydrophobicity, thus potentially reducing its dependence on polar sites. A significant negative correlation was observed between Q_e of LDNA and the average pore diameter of biochars, whereas the correlation was not significant for sDNA. This result suggested a potential link to steric hindrance for the larger LDNA on biochars, whereas sDNA readily accessed the mesopores (> 20 nm). Additionally, the adsorption of LDNA was impeded by electrostatic repulsion, resulting from its high negative charge, which aligned with its significant positive correlation with Zeta potential.

The desorption rate of sDNA and LDNA on tested biochars with different desorption agents were shown in Fig. 4 (c-f). Background solution was utilized for baseline desorption to characterize the contribution of weak physical adsorption to the binding process. When the background solution (Tris-HCl) acted as desorption reagent, the desorption ratio of sDNA was higher than that of LDNA, indicating that the affinity between DNA and biochar was strengthened with increasing DNA chain length. NaOH could enhance electrostatic repulsion between negatively charged DNA and biochars. NaOH exhibited the highest desorption extent for sDNA, and the desorption rates of sDNA decreased with increasing pyrolysis temperature: BC300 (60.51%) ≈ BC400 (61.07%) > BC500 (42.77%) > BC600 (25.39%). The similar trend of LDNA desorption by NaOH showed the order of BC300 (66.98%) ≈

BC400 (59.86%) > BC500 (21.35%) > BC600 (5.03%). Phosphate competed for the covalent binding between biochars and the phosphate backbones of DNA. When PO_4^{3-} was applied as the desorption agent, the desorption rates of sDNA were similar with LDNA on all biochars. The ligand binding sites between biochar and DNA were less sensitive to DNA length. Urea and 20% methanol inhibited H-bonding interactions involving N_2H_2 and -OH functionalities, respectively. When urea and 20% methanol were used as desorption reagent, the desorption rate of sDNA from low-temperature biochar was lower than that of LDNA, whereas the opposite trend was observed for high-temperature biochar. This difference could be attributed to the distinct surface properties of biochars. Low-temperature biochar contained a great abundance of oxygen-containing functional groups, which facilitate interactions with DNA primarily through hydrogen bonding. In contrast, high-temperature biochar exhibited strong hydrophobicity, leading to a great reliance on hydrophobic interactions with DNA.

Understanding the immobilization of eDNA on biochar was fundamentally important for evaluating its environmental fate, particularly its migration potential and bioavailability. Two cycles of desorption experiments were conducted for sDNA and LDNA after loading on biochars and desorption hysteresis was observed (Fig. S4). The release rate (RR) was calculated based on the equation shown in Text S1. RR values of sDNA and LDNA on BC300 increased with an increment in solid-phase loading (Fig. 5). This concentration-dependent releasing phenomenon could be attributed to the heterogeneous distribution of sorption site energy on BC300. The DNA preferentially occupied high-energy sorption sites and then randomly sorbed on the sites with low energy (Li et al., 2025). The adsorption of sDNA and LDNA on BC400, BC500 and BC600 was stable with low RR values (almost zero). This might be due to the highly hydrophobicity and aromaticity of these biochars, which hindered the desorption of DNA. Furthermore, it was observed that LDNA exhibited a greater desorption hysteresis than sDNA. This phenomenon could be attributed to the multisite anchoring of LDNA on the biochar surface, which consequently enhances adsorption strength and stability. The low RR values of adsorbed sDNA and LDNA on biochar indicated that the adsorption of DNA on biochar was irreversible, which might protect DNA from enzymatic degradation (Brundin et al., 2013), thereby increasing the persistence of DNA in the environment.

3.5. The structure and stability of adsorbed DNA on biochar

The configuration change of sDNA and LDNA after binding with biochar was examined by FTIR. The FTIR spectra of biochars before and after DNA attachment were depicted in Fig. 6 (a) and (b). The peaks at 1054 and 1036 cm^{-1} were ascribed to C-C/C-O symmetric stretching vibrations representing the carbohydrate skeleton of DNA. It was evident that two peaks appeared at 1296 and 3186 (sDNA, Fig. 6 (a))/ 3230 (LDNA, Fig. 6 (b)) cm^{-1} after DNA adsorption on biochars, which confirmed that hydrogen bonds were formed between the nitrogenous bases in DNA and nitrogenous or oxygen-containing functional groups on biochar surface (Banyay et al., 2003). After the adsorption process, C=O (1698 cm^{-1}) and C=C (1591 cm^{-1}) stretching variation became broader and stronger. These changes provide spectroscopic for hydrogen bonding and π-π interactions occurring between DNA and biochar. Compared with the FTIR spectra of free DNA (Fig. S1), the absorption band at 1227 and 1085 cm^{-1}, which represented the stretch vibration of PO^{2-}, disappeared after adsorption.

FTIR spectrum of adsorbed DNA by subtracting the IR spectra of individual biochar from those of biochar-DNA complexes. The synchronous FTIR 2D-COS analyses of bound sDNA and LDNA were employed to clearly identified the conformational changes of DNA. The synchronous maps of sDNA on test biochars (Fig. 6 (c-f)) showed four predominant autopeaks at 1630-1690 cm^{-1}(b), 1010-1090 cm^{-1} (d), 1200-1250 cm^{-1} (c) and 760-780 cm^{-1} (e), listed in descending order of intensity. The presence of these autopeaks directly indicated the functional groups that were perturbed during adsorption (Table S1). The red shift observed in out-of-plane base vibrational bands (783→760-780 cm^{-1}). These changes indicates that the conformation of sDNA had undergone a slight alteration. Two main autopeaks (1565-1580 and 1350-1360 cm^{-1}) were displayed in the synchronous maps of LDNA on test biochars (Fig. 6 (g-j)), suggesting that the C=C, C-N and C-H of DNA were disturbed when adsorption.

DNA was susceptible to oxidative damage by free radicals. We measured the signals of ·OH, $O_2^{\cdot-}$ (Fig. S5(a)), and persistent free radicals (Fig. S5(b)) in biochars before and after reacting with DNA. It was found that the signal changes in biochars after reacting with DNA were almost negligible., indicating that these free radicals were unlikely to participate in reactions with DNA. To further verify the structural integrity of DNA after adsorption, the DNA desorbed from biochar was subjected to gel electrophoresis analysis (Fig. S5(c)). The bright bands of sDNA and LDNA was unchanged after adsorption on test biochars, confirming that the DNA was not fragmented. Lian et al. also observed that free radicals in bulk biochar played a negligible role in destroying DNA (Lian et al., 2020). However, the subtle changes in DNA bases and phosphate backbone were observed in synchronous FTIR 2D COS. These results suggested that DNA binding to biochar affected its secondary conformation without causing chain fragment. Adsorption of DNA onto materials had been shown to protect DNA from enzymatic degradation (Fang et al., 2021; Schefer et al., 2025). Previous studies showed that the enzymatic degradation of DNA was not governed by the affinity of DNA adsorption on minerals (Cai et al., 2006). The protection of DNA by soil particles against enzymatic degradation was that the binding of DNA on adsorbents altered the conformation of DNA (Cai et al., 2006; Heddi et al., 2010). Consequently, changes in DNA structure after binding on biochar might prevent nucleases from recognizing or interacting with appropriate binding or cleavage sites on the DNA, thereby prolonging the environmental persistence of DNA.

In order to further analyze the stability of sDNA and LDNA secondary

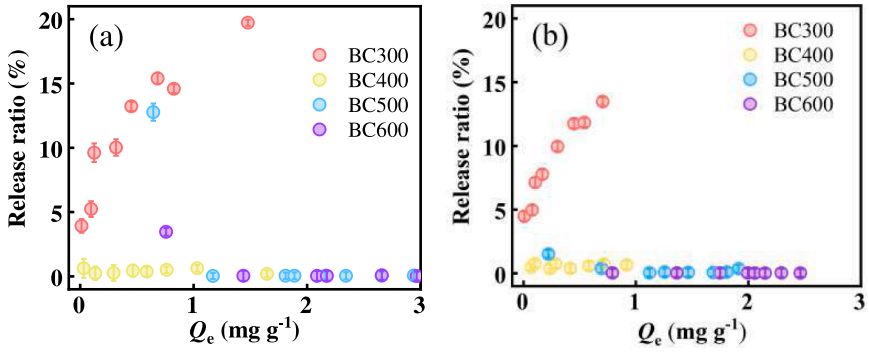

Fig. 5. Release ratio of the adsorbed sDNA (a) and LDNA (b) after two desorption steps. Data points and error bars represented the mean and standard deviation of triplicates run in parallel.

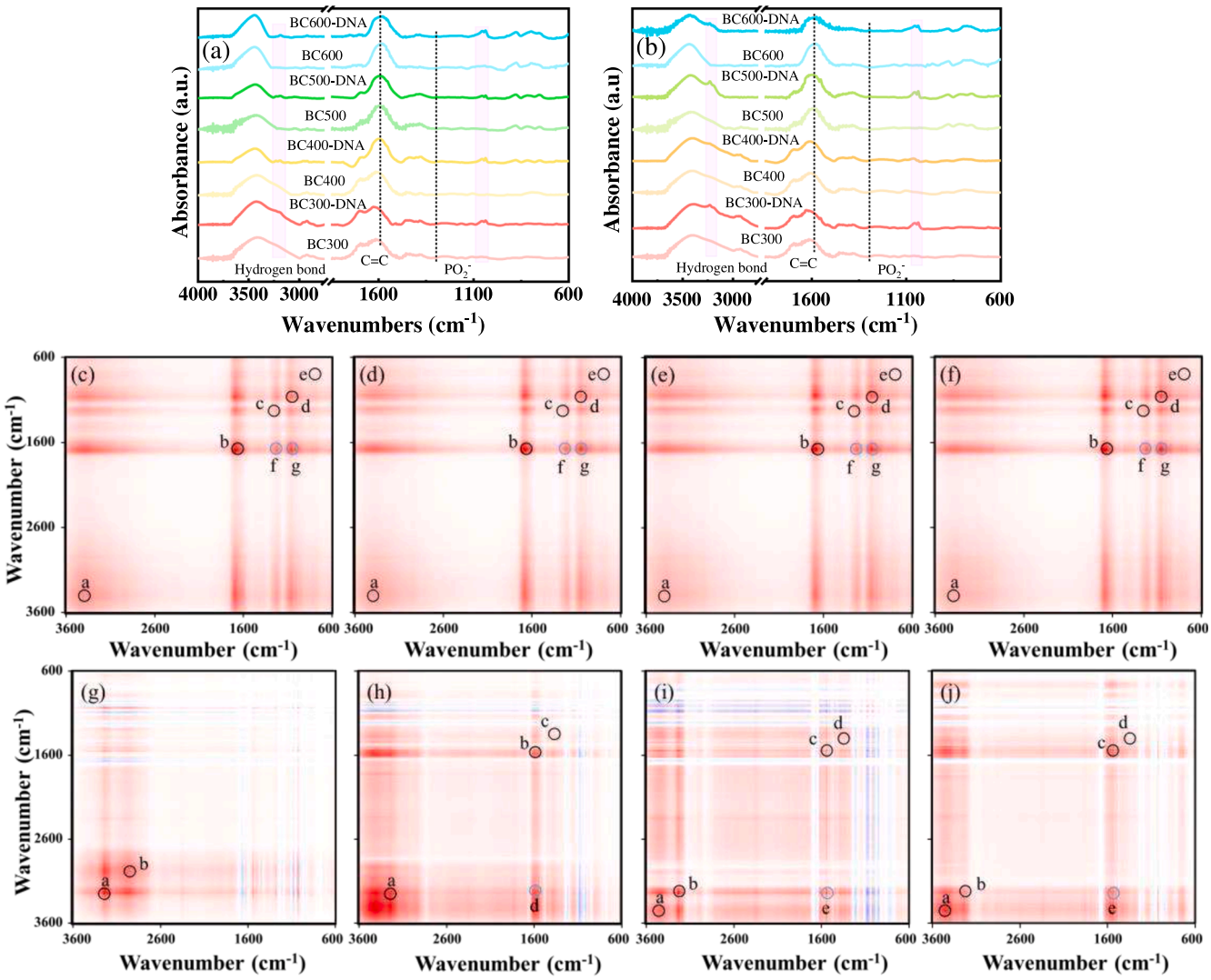

Fig. 6. The FTIR spectra of biochars before and after the sorption of sDNA (a) and LDNA (b). The synchronous FTIR 2D-COS maps of sDNA (c-f) and LDNA (g-j) before and after adsorption on BC300 (c, g), BC400 (d, h), BC500 (e, i) and BC600 (f, j).

structure during adsorption, we calculated the time evolution of the root mean square deviation (RMSD) (Fig. 7 (a)), the number of hydrogen bonds (Fig. 7 (b)) and π-π stacking (Fig. 7 (c)) in dsDNA. The RMSD quantified the overall structural deviation of a molecule from its initial conformation over time. A low and stable RMSD values implied the molecule was maintaining its structural integrity, whereas a high or continuously increasing RMSD revealed significant instability and large-scale conformational dynamics (Liu et al., 2020). The number of hydrogen bonds between base pairs served as a direct measure of the integrity and stability of the double-helix structure (Zhou et al., 2021). The number of π-π stacking interactions reflected the compactness and coaxial stability of the DNA base stack. We found that the adsorption mechanisms of DNA with biochar were mainly π-π interactions and hydrogen bonds. Similar interaction mechanisms were also observed on graphene oxide (GO) (Al Umairi et al., 2025; Zeng et al., 2015). Therefore, we used GO as a simplified proxy for biochar aromatic surfaces. Due to the lack of complex structure in GO model, the MD results provided qualitative mechanistic insights into DNA-biochar π-π/hydrogen bonding interactions rather than quantitative representation of real biochar systems. For example, the DNA conformational changes induced by ash and surface heterogeneity might be overlooked, which could lead to the underestimation of simulation results. Nevertheless, it could provide valuable insights by addressing the influence of adsorption on DNA conformation with different lengths. 12 bp DNA and 40 bp were used to represent sDNA and LDNA respectively because of the limitation of molecular size in the simulation.

As seen in Fig. 7 (a), the RMSD values of sDNA and LDNA rapidly increased to 0.48 and 0.9 nm at about 5 ns, respectively. The RMSD of LDNA existed a larger floating up and down compare with that of sDNA. To better understand this fluctuation, we tracked the molecular trajectory of sDNA and LDNA from their initial localization in solution to their final adsorption equilibrium on GO surface. In the trajectory snapshot of sDNA and LDNA, as shown in Fig. 7 (d) and (e), it was found that sDNA and LDNA could stably adsorbed on GO surface through the nucleobases at the terminus. With increasing length, the flexibility of dsDNA molecules also increased (Wu et al., 2023). DNA molecules with high flexibility could exhibit RMSD fluctuation due to the overall structural changes during the adsorption dynamics of dsDNA molecules on GO surface.

The intra-molecular hydrogen bonds of dsDNA molecules were especially important for maintaining its double-helix structure. During the simulation, the number of hydrogen bonds of sDNA decreased from an initial value of approximately 26 to a final value of about 18, with a retention rate of 69.23% (Fig. 7 (b)). LDNA retained 80.22% of its initial hydrogen bonds, with the count decreasing from approximately 91 to 73. LDNA exhibited better hydrogen bond stability and structural

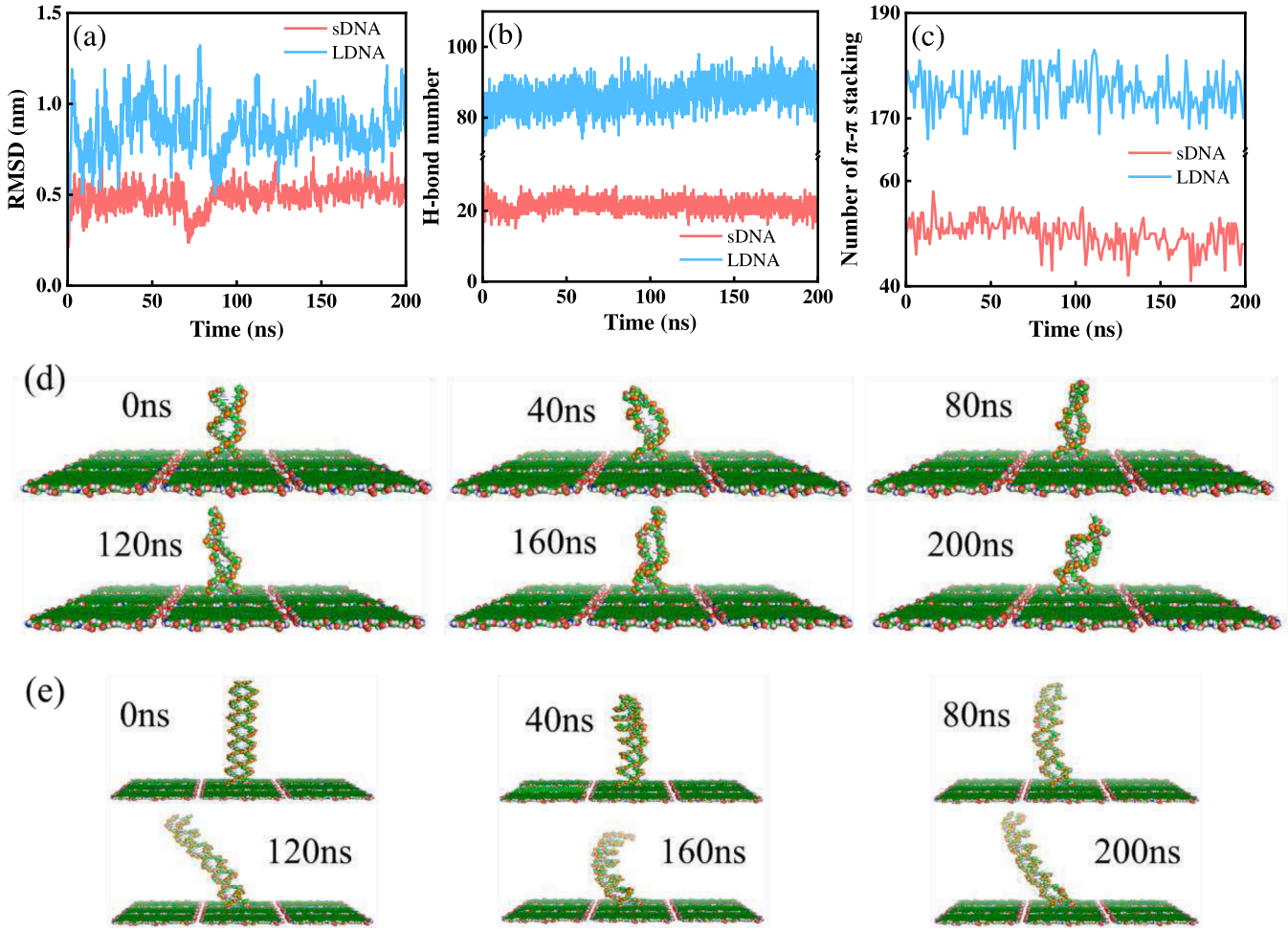

Fig. 7. The RMSD values of sDNA and LDNA as a function of simulation time (a). The numbers of intra-molecular hydrogen bonds (b) and π-π stacking (c) in sDNA and LDNA. The trajectory snapshot of sDNA (d) and LDNA (e) adsorbed on GO surface.

integrity during the simulation process, while the terminal bases of sDNA was relatively more prone to hydrogen bond breakage and structural loosening. The MD simulations revealed a decline in base-staking interaction, from 54 to 48 in sDNA and from 179 to 170 in LDNA (Fig. 7 (c)). This relative lability of the short DNA's ends highlights the role of chain length in stabilizing π-π stacking. The above results indicated that LDNA systems had good structural stability, but the stability of sDNA was relatively weak.

We calculated the angle between the central axis of the base pairs in ds-DNA and GO surface as shown in Fig. S6. The angles in sDNA and LDNA systems during the final 60 ns of simulation were 72.74° and 45.15°, respectively. The angle change was caused by the π-π interaction between DNA bases and GO. The high flexibility gave the adsorbed LDNA molecules more chance to contact the GO surface with their free terminals compared to sDNA. The smaller angle of LDNA system suggested a stronger binding with GO compare with sDNA. The results further confirmed that the reduced desorption and release rate of LDNA.

4. Conclusion

This study systematically elucidated the adsorption behaviors and mechanisms of sDNA and LDNA on biochars under neutral pH conditions, revealing critical insights governed by DNA length and biochar properties. sDNA exhibited a higher adsorption capacity due to its superior accessibility to internal mesopores, while LDNA, facing steric limitations, adsorbed primarily on external surfaces but forms stronger and more stable complexes via multisite anchoring. The adsorption was primarily driven by π-π interactions and hydrophobic forces. The increased aromaticity and specific surface area of high-temperature biochars (BC500 and BC600) significantly enhanced adsorption. The adsorbed DNA underwent mild conformational changes (base stacking disorder and hydrogen bond breakage of the terminal bases) but retained strand integrity, with LDNA showing greater structural stability than sDNA. The environmental fate of DNA was critically determined by the interplay between its molecular length and the structural and chemical characteristics of the surrounding biochar. These findings provided insights into the relative preservation of different DNA lengths in environmental systems, particularly the preservation of short DNA fragments (<100 bp) over long-term periods.

Implications, limitation and outlook

This study provides critical mechanistic insights into the role of DNA length for DNA adsorption onto biochar surfaces and the stability of DNA after adsorption. Our findings demonstrate that DNA undergoes irreversible adsorption onto biochar and accompanied by conformational changes, which may protect DNA from enzymatic degradation (Brundin et al., 2013; del Valle et al., 2014). Our results have direct and significant implications for understanding the fate and persistence of DNA in natural environments. For instance, the low desorption efficiency of DNA from biochar may lead to underestimation of species distributions and complicating DNA-based biodiversity monitoring. When DNA was adsorbed on biochar, its detectability may be educed, potentially leading to false negatives in environmental assessments.

Based on our data, we can be inferred that the application of high-temperature biochar may facilitate the enrichment of DNA in the environment, rendering biochar a DNA sink. Under neutral conditions, the adsorption capacity of short DNA onto biochar is significantly higher than that of long DNA. This discovery offers a vital basis for elucidating the environmental preservation rules of DNA with varying lengths, and particularly reveals the long-term preservation characteristics of short DNA in the environment. Furthermore, it is noteworthy that carbon-based materials originally intended for DNA degradation may conversely promote horizontal gene transfer of DNA from a long-term environmental perspective. Due to the slow adsorption rate of highly degraded DNA and the fact that 20 bp DNA can be acquired by bacteria through natural transformation alone (Overballe-Petersen et al., 2013). Compared with mineral, biochar exhibits weaker DNA adsorption capacity, indicating that biochar may not be suitable for broad-spectrum DNA capture scenarios. However, our findings also highlight the importance of tailoring biochar properties according to target DNA length to adapt to specific application scenarios. For the capture of trace short DNA, high-temperature biochar represents a more ideal option; whereas in scenarios requiring controlled DNA release (e.g., gene delivery systems), low-temperature biochar may demonstrate superior applicability.

It should be noted that the experimental conditions employed in this study do not fully replicate the complexity of real environments. The solution environment conditions (e.g., the presence of multivalent ions, pH fluctuations, and variations in ionic strength) may induce DNA conformational changes, thereby affecting its adsorption behavior on biochar surfaces (Sheng et al., 2019; Wang et al., 2025). The coexisting organics and inorganics in natural environments may reduce DNA adsorption through competitive adsorption (Müller et al., 2024). Although herring sperm DNA and salmon sperm DNA are commonly employed model DNA, they cannot fully represent the diversity of fragment sizes and conformations of DNA in natural environments, potentially leading to an incomplete assessment of the effects of DNA types on adsorption and degradation processes (Mauvisseau et al., 2022). In addition, biochar undergoes an aging process after entering natural environments, which increases the number of surface oxygen-containing functional groups (Long et al., 2024), enhances surface roughness (Wang et al., 2021), and reduces particle size (Spokas et al., 2014). These changes in physicochemical properties of biochar may significantly impact the adsorption and stability of DNA. The aged biochar may enhance DNA adsorption capacity and reduce the enzymes accessibility of adsorbed DNA. The current study used model systems to systematically understand fundamental processes, which simplified environmental conditions; nevertheless, it can provide valuable insights by focusing on the key influencing factors during the adsorption process. Future research could further expand to investigate the adsorption behavior of DNA on carbon-based materials under diverse environmental conditions, systematically exploring the regulatory effects of factors such as pH, ion type and concentration, and coexisting organic matter, to achieve a more comprehensive understanding of the interaction mechanisms between DNA and biochar. Moreover, this study only investigates the adsorption-desorption equilibrium and conformational changes of DNA, without directly evaluating the subsequent biological effects of adsorbed DNA. Although biochar-mediated DNA adsorption and conformational changes may prolong the environmental persistence of DNA, this does not equate to ensuring its bioavailability, nor can it directly infer the extent to which the sensitivity of DNA to enzymatic degradation is reduced in complex media. Therefore, in-depth exploration of the biological consequences of adsorbed DNA is of great significance. Research in this direction will provide key scientific evidence for optimizing biodiversity monitoring methods and assessing the risks of genetic material transfer in the environment.

CRediT authorship contribution statement

Xiao Sun: Writing – original draft, Investigation, Data curation. **Lin Shi:** Writing – review & editing, Methodology, Investigation. **Huang Zhang:** Formal analysis. **Fangfang Li:** Writing – review & editing, Funding acquisition. **Yanjin Long:** Data curation. **Di Zhang:** Writing – review & editing, Investigation, Funding acquisition.

Declaration of competing interest

The authors declare that they have no known competing financial interests or personal relationships that could have appeared to influence the work reported in this paper.

Acknowledgements

This work was supported by the Taishan Scholar Foundation of Shandong Province (tsqn202306276), Natural Science Foundation of China (42167030), Natural Science Foundation of Shandong Province (ZR2022QD088), and Linyi University High-level Talents (Doctor) Research Foundation (Z6122037, Z6122025).

Supplementary materials

Supplementary material associated with this article can be found, in the online version, at doi:10.1016/j.wroa.2026.100496.

Data availability

Data will be made available on request

References

Al Umairi, B.S., Clarke, D.J., Bichenkova, E.V., 2025. NMR insights into nanoscale molecular interactions between nucleic acids and pristine graphene in aqueous solution. Biomacromolecules 26, 7852–7865.
Ballard, J.W.O., Whitlock, M.C., 2004. The incomplete natural history of mitochondria. Mol. Ecol. 13, 729–744.
Banyay, M., Sarkar, M., Gräslund, A., 2003. A library of IR bands of nucleic acids in solution. Biophys. Chem. 104, 477–488.
Blackman, R., Couton, M., Keck, F., Kirschner, D., Carraro, L., Cereghetti, E., Perrelet, K., Bossart, R., Brantschen, J., Zhang, Y., Altermatt, F., 2024. Environmental DNA: The next chapter. Mol. Ecol. 33, 17355.
Brundin, M., Figdor, D., Sundqvist, G., Sjögren, U., 2013. DNA Binding to Hydroxyapatite: A Potential Mechanism for Preservation of Microbial DNA. J. Endodont. 39, 211–216.
Cai, P., Huang, Q.Y., Zhang, X.W., 2006. Interactions of DNA with clay minerals and soil colloidal particles and protection against degradation by DNase. Environ. Sci. Technol. 40, 2971–2976.
Chen, H., Li, W., Wang, J., Xu, H., Liu, Y., Zhang, Z., Li, Y., Zhang, Y., 2019. Adsorption of cadmium and lead ions by phosphoric acid-modified biochar generated from chicken feather: Selective adsorption and influence of dissolved organic matter. Bioresour. Technol. 292, 121948.
Chen, H.Y., Yang, X.J., Liu, Y.L., Lin, X.M., Wang, J.J., Zhang, Z., Li, N., Li, Y.T., Zhang, Y.L., 2021. KOH modification effectively enhances the Cd and Pb adsorption performance of N-enriched biochar derived from waste chicken feathers. Waste Manage. 130, 82–92.
Cochran, J.P., Zhang, L.Y., Parrott, B.B., Seaman, J.C., 2024. Plasmid size determines adsorption to clay and breakthrough in a saturated sand column. Heliyon 10, 29679.
del Valle, L.J., Bertran, O., Chaves, G., Revilla-López, G., Rivas, M., Casas, M.T., Casanovas, J., Turon, P., Puiggalí, J., Alemán, C., 2014. DNA adsorbed on hydroxyapatite surfaces. J. Mater. Chem. B 2, 6953–6966.
Fan, L., Zhou, X., Liu, Q., Wan, Y., Cai, J., Chen, W., Chen, F., Ji, L., Cheng, L., Luo, H., 2019. Properties of *eupatorium adenophora* spreng (crofton weed) biochar produced at different pyrolysis temperatures. Environ. Eng. Sci. 36, 937–946.
Fang, J., Jin, L., Meng, Q.K., Wang, D.J., Lin, D.H., 2021. Interactions of extracellular DNA with aromatized biochar and protection against degradation by DNase I. J. Environ. Sci. 101, 205–216.
Hao, J.H., Zhang, X., Zong, S.J., Zhuo, Y., Zhang, Y., Wang, S., Deng, Y., Zhang, X.K., Li, J., 2024. Biochar as a highly efficient adsorption carrier for sewage sludge-derived nutrients and biostimulants: Component fixation and mechanism. Biochar 6, 42.
He, Y.W., Yin, X.W., Li, F.H., Wu, B., Zhu, L., Ge, D.B., Wang, N.Y., Chen, A.W., Zhang, L. H., Yan, B.H., Huang, H.L., Luo, L., Wu, G.Y., Zhang, J.C., 2023. Response characteristics of antibiotic resistance genes and bacterial communities during

agricultural waste composting: Focusing on biogas residue combined with biochar amendments. Bioresour. Technol. 372, 128636.
Heddi, B., Abi-Ghanem, J., Lavigne, M., Hartmann, B., 2010. Sequence-dependent DNA flexibility mediates DNase I cleavage. J. Mol. Biol. 395, 123–133.
Hu, Z.T., Ding, Y., Shao, Y., Cai, L., Jin, Z.-Y., Liu, Z., Zhao, J., Li, F., Pan, Z., Li, X., Zhao, J., 2021. Banana peel biochar with nanoflake-assembled structure for cross contamination treatment in water: Interaction behaviors between lead and tetracycline. Chem. Eng. J. 420, 129807.
Kjaer, K.H., Pedersen, M.W., De Sanctis, B.S., De Cahsan, B.S., Korneliussen, T.S.K., Michelsen, C.S., Sand, K.K.H., Jelavic, S., Ruter, A.H.K., Schmidt, A.M.A.S., Kjeldsen, K.K., Tesakov, A.S.C., Snowball, I.G., Gosse, J.C., Alsos, I.G., Wang, Y., Dockter, C.E., Rasmussen, M., Jorgensen, M.E., Skadhauge, B., Prohaska, A., Kristensen, J.A., Bjerager, M., Allentoft, M.E., Coissac, E., Rouillard, A., Simakova, A., Fernandez-Guerra, A., Bowler, C., Macias-Fauria, M., Vinner, L., Welch, J.J., Hidy, A.J., Sikora, M., Collins, M.J., Durbin, R., Larsen, N.K., Willerslev, E., PhyloNorway, C., 2022. A 2-million-year-old ecosystem in Greenland uncovered by environmental DNA. Nature 612, 283. -+.
Lee, J., Yim, Y., Kim, S., Choi, M.H., Choi, B.-S., Lee, Y., Min, D.H., 2016. In-depth investigation of the interaction between DNA and nano-sized graphene oxide. Carbon 97, 92–98.
Li, J., Yang, Y., Liang, N., Wang, X., Tong, X., Pan, B., 2025. Sustainable fabrication of hierarchical porous graphitic carbon from banana peduncle via self-template and self-activation for high-performance sorption of phthalate easters. Sep. Purif. Technol. 375, 133657.
Lian, F., Yu, W.C., Zhou, Q.X., Gu, S.G., Wang, Z.Y., Xing, B.S., 2020. Size matters: Nano-biochar triggers decomposition and transformation inhibition of antibiotic resistance genes in aqueous environments. Environ. Sci. Technol. 54, 8821–8829.
Liu, F., Zhang, Y., Wang, H., Li, L., Zhao, W., Shen, J.W., Liang, L., 2020. Study on the adsorption orientation of DNA on two-dimensional MoS_2 surface via molecular dynamics simulation: A vertical orientation phenomenon. Chem. Phys. 529, 110546.
Long, X.X., Yu, Z.N., Liu, S.W., Gao, T., Qiu, R.L., 2024. A systematic review of biochar aging and the potential eco-environmental risk in heavy metal contaminated soil. J. Hazard. Mater. 472, 134345.
Lv, Z., Wang, Z., Wang, H., Li, J., Li, K., 2024. Adsorption of cationic/anionic dyes and endocrine disruptors by yeast/cyclodextrin polymer composites. RSC Adv. 14, 6627–6641.
Mauvisseau, Q., Harper, L.R., Sander, M., Hanner, R.H., Kleyer, H., Deiner, K., 2022. The multiple states of environmental DNA and what is knownabout their persistence in aquatic environments. Environ. Sci. Technol. 56, 5322–5333.
Müller, N.D., Kirtane, A., Schefer, R.B., Mitrano, D.M., 2024. eDNA Adsorption onto microplastics: Impacts of water chemistry and polymer physiochemical properties. Environ. Sci. Technol. 58, 7588–7599.
Nguyen, T.H., Elimelech, M., 2007. Plasmid DNA adsorption on silica: Kinetics and conformational changes in monovalent and divalent salts. Biomacromolecules 8, 24–32.
Overballe-Petersen, S., Harms, K., Orlando, L.A.A., Mayar, J.V.M., Rasmussen, S., Dahl, T.W., Rosing, M.T., Poole, A.M., Sicheritz-Ponten, T., Brunak, S., Inselmann, S., De Vries, J., Wackernagel, W., Pybus, O.G., Nielsen, R., Johnsen, P.J., Nielsen, K.M., Willerslev, E., 2013. Bacterial natural transformation by highly fragmented and damaged DNA. PNAS 110, 19860–19865.
Qi, L., Tang, X., Wang, Z., Peng, X., 2017. Pore characterization of different types of coal from coal and gas outburst disaster sites using low temperature nitrogen adsorption approach. Int. J. Min. Sci. Technol. 27, 371–377.
Sawyer, S., Krause, J., Guschanski, K., Savolainen, V., Pääbo, S., 2012. Temporal patterns of nucleotide misincorporations and dna fragmentation in ancient DNA. Plos One 7, 34131.
Schefer, R.B., Paolucci, C., Mitrano, D.M., 2025. Adsorption and protection of environmental DNA (eDNA) on polymer and silica surfaces. Environ. Sci. Technol. 59, 19479–19489.
Shao, B.B., Liu, Z.F., Tang, L., Liu, Y., Liang, Q.H., Wu, T., Pan, Y., Zhang, X.S., Tan, X.F., Yu, J.F., 2022. The effects of biochar on antibiotic resistance genes (ARGs) removal during different environmental governance processes: A review. J. Hazard. Mater. 435, 129067.
Sheng, X., Qin, C., Yang, B., Hu, X.J., Liu, C., Waigi, M.G., Li, X.L., Ling, W.T., 2019. Metal cation saturation on montmorillonites facilitates the adsorption of DNA via cation bridging. Chemosphere 235, 670–678.
Shi, L., Zhang, D., Yang, M.Y., Li, F.F., Zhao, J.F., He, Z.H., Bai, Y.W., 2024. New discovery of extremely high adsorption of environmental DNA on cuttlefish bone pyrolysis derivative via large pore structure and carbon film. Waste Manage. 175, 286–293.
Song, Q.Q., Kong, F.Y., Liu, B.F., Song, X.T., Ren, H.Y., 2024. Biochar-based composites for removing chlorinated organic pollutants: Applications, mechanisms, and perspectives. Environ. Sci. Ecotechnol. 21, 100420.
Spokas, K.A., Novak, J.M., Masiello, C.A., Johnson, M.G., Colosky, E.C., Ippolito, J.A., Trigo, C., 2014. Physical disintegration of biochar: An overlooked process. Environ. Sci. Technol. Lett. 1, 326–332.
Sun, K., Kang, M., Zhang, Z., Jin, J., Wang, Z., Pan, Z., Xu, D., Wu, F., Xing, B., 2013. Impact of deashing treatment on biochar structural properties and potential sorption mechanisms of phenanthrene. Environ. Sci. Technol. 47, 11473–11481.
Teng, T.P., Chang, S.C., Chen, Z.Y., Huang, C.K., Tseng, S.F., Yang, C.R., 2019. High-yield production of graphene flakes using a novel electrochemical/mechanical hybrid exfoliation. Int. J. Adv. Manuf. Technol. 104, 2751–2760.
Viet Cuong, D., Chia-Hung, H., Thuy Ninh, D., 2022. O, N-doped porous biochar by air oxidation for enhancing heavy metal removal: The role of O, N functional groups. Chemosphere 293, 133622.
Wang, C.Z., Liu, G., McNew, C.P., Volkmann, T.H.M., Pangle, L., Troch, P.A., Lyon, S.W., Kim, M., Huo, Z.L., Dahlke, H.E., 2022. Simulation of experimental synthetic DNA tracer transport through the vadose zone. Water Res 223, 119009.
Wang, K.F., Peng, N., Niu, X.C., Lu, G.N., Zhong, Y.M., Yu, X.L., Du, C., Gu, J.F., Zhou, H. J., Sun, J.T., 2021. Effects of aging on surface properties and endogenous copper and zinc leachability of swine manure biochar and its composite with alkali-fused fly ash. Waste Manage 126, 400–410.
Wang, X., Wang, Y., Gao, M.Y., Hou, F.Y., Wang, J.X., Wang, J.Y., Li, Y., Wang, Z.B., 2025. Synergistic regulation of DNA morphology by metal cations and low pH. Microsc. Res. Tech. 88, 696–704.
Wu, C.Y., Fu, L.Y., Li, H.Q., Liu, X., Wan, C.L., 2022. Using biochar to strengthen the removal of antibiotic resistance genes: Performance and mechanism. Sci. Total Environ. 816, 151554.
Wu, M., Ma, H., Fang, H., Yang, L., Lei, X., 2023. Adsorption dynamics of double-stranded DNA on a graphene oxide surface with both large unoxidized and oxidized regions. Chin. Phys. B. 32, 018701.
Wu, X.X., Tang, Z.R., Li, Y.Q., Du, Z., Li, W., Wang, S.M., Huang, C.H., 2025. Biochar promotes removal of intracellular and extracellular antibiotic resistance genes in sludge compost: Reshaping microbial communities. J. Environ. Manage. 392, 126781.
Xiao, X., Chen, B.L., Chen, Z.M., Zhu, L.Z., Schnoor, J.L., 2018. Insight into multiple and multilevel structures of biochars and their potential environmental applications: A critical review. Environ. Sci. Technol. 52, 5027–5047.
Yang, M.Y., Shi, L., Zhang, D., He, Z.H., Liang, A.P., Sun, X., 2022a. Adsorption of herring sperm DNA onto pine sawdust biochar: Thermodynamics and site energy distribution. Front. Environ. Sci. Eng. 16, 144.
Yang, Y., Sun, K., Han, L.F., Chen, Y.L., Liu, J., Xing, B.S., 2022b. Biochar stability and impact on soil organic carbon mineralization depend on biochar processing, aging and soil clay content. Soil Biol. Biochem. 169, 108657.
Yu, W.C., Zhan, S.H., Shen, Z.Q., Zhou, Q.X., Yang, D., 2017. Efficient removal mechanism for antibiotic resistance genes from aquatic environments by graphene oxide nanosheet. Chem. Eng. J. 313, 836–846.
Zeng, S., Chen, L., Wang, Y., Chen, J., 2015. Exploration on the mechanism of DNA adsorption on graphene and graphene oxide via molecular simulations. J. Phys. D: Appl. Phys. 48, 275402.
Zhang, M.L., Liu, J.C., Zhang, W.F., Feng, M.B., Yu, X., Ye, C.S., 2024. Neglected contributors to the transmission of bacterial antibiotic resistance in drinking water: Extracellular antibiotic resistance genes and the natural transformation. Sci. Total Environ. 953, 175970.
Zhang, Y.R., Hartung, M.B., Hawkins, A.J., Dekas, A.E., Li, K.W., Horne, R.N., 2021. DNA tracer transport through porous media-the effect of dna length and adsorption. Water Resour. Res. 57, 2020WR028382.
Zhou, H., Xie, Z.-X., Liang, L., Zhang, P., Ma, X., Kong, Z., Shen, J.-W., Hu, W., 2021. Theoretical investigation on the adsorption orientation of DNA on two-dimensional $MoSe_2$. Chem. Phys. 551, 111329.